Characterization Method of Radiated Magnetic Field Based on Integrated Antenna Measurement Applied to Power Module Technologies

Guillaume Vine, Paul-Etienne Vidal, and Jean-Marc Dienot, *Member, IEEE*

***Abstract*—This paper deals with near magnetic field characterization of power electronic modules. The purpose is to relate near-field (NF) measurement to switching behavioral characteristics. An elementary magnetic sensor is presented and its characterization is detailed. Isolated antenna simulations are computed, thanks to an equivalent lumped parameter model of the antenna. Experimental characterizations are also provided to be compared to simulations. Following that, the characterized antenna is integrated into a specific power electronic device. NF measurements allow us to compute magnetic field mappings of the device under test. Time and frequency analyses of the sensor output data are discussed based on current measurements and magnetic simulation of the power electronic device. Finally, NF measurement enables access to switching details, disturbance propagation paths, and radiation distribution of a power electronic module.**

***Index Terms*—Electromagnetic characterization, near-field (NF) scanning, power electronic.**

I. Introduction

FOR an electrical power conversion, the power to volume ratio, the efficiency, and the cooling are some of the most studied problems. Because of the improvement in integration technology, and the progressive maturity of wide-bandgap, SiC, and GaN semiconductors, the power electronics structure has changed from planar to a three-dimensional (3-D) highly integrated structure [1]. Indeed, to fulfill new density requirements, switching frequencies, current, and voltage magnitudes have increased, among other variables. This leads to consider the electromagnetic (EM) interference emitted by the power electronics equipment, as a key study for further improvements.

Current flows and potential variations induce EM fields in electrical circuits. In power electronic modules, high currents and voltages, combined with very short switching times, produce wideband EM radiations that have been characterized until 1 GHz [1], [2]. In a specific region, denoted the near-field (NF) region, magnetic and electric fields are decoupled. In such a case, the magnetic field is mainly associated with current flows, and the electric field with electric potential variations [3]. The magnetic and electric field measurement techniques in this region have attracted a lot of attention because of their high resolution and non-invasive aspect. They are usually based on the displacement of the device under test (DUT) or incremental measurement probes, using a mechanical positioning system. This provides access to the electromagnetic mapping of the DUT and gives relevant information on its electrical behavior including amongst others the localization of high radiation areas and the estimation of conducted disturbances [4], [5].

However, the main limitation of a mechanical positioning system is the sweeping time needed to acquire all the measurements. The large dimensions of devices in power electronics require scanning steps and characterization times that are incompatible with an *in situ* measurement. Consequently, the NF measurement in power modules requires placing the sensor within the plastic packaging boundary, and close to the emission sources. The proposed alternative is to consider a design and integration of NF probes within the power modules. On the one hand, significant reductions in measurement time can be achieved. On the other hand, potential evolutions of the DUT electrical behavior during the operating cycle could be measured and analyzed. This paper is a step of a general framework, which targets to monitor some potential failure modes in real time.

Previous works on this topic, started in 2005, showed its feasibility on industrial power modules [6]. Following them, dedicated magnetic probes were developed with a particular attention on control of the coupling factors, noise rejection, and frequency bandwidth [7]. Nowadays, NF measurements are applied to fault detection or conducted emissions' characterization of power modules [8]. Finally, this paper deals with the next step, which is about the application of NF probes in power electronic environment, obtained measurements, and measurement analysis.

Section II details the loop passive antenna associated with the measurement setup. Sensor performances related to magnetic NF measurement are discussed. Section III is about the modeling of the measurement setup, including the antenna. A simplified power module, the experimental test bench, and its measurement process are described in Section IV. Finally, Section V presents

Manuscript received August 29, 2018; revised November 20, 2018, February 12, 2019, and April 12, 2019; accepted April 26, 2019. Date of publication May 9, 2019; date of current version November 12, 2019. This work was supported by the French National Research Agency for Science. It is a research theme of the Project CAPTIF—Embedded innovative sensors and software in power electronic components—ANR-14-CE05-0044. Recommended for publication by Associate Editor F. Costa. *(Corresponding author: Paul-Etienne Vidal.)*

G. Vine and P.-E. Vidal are with the Laboratoire Genie de Production-Ecole Nationale d'Ingenieurs de Tarbes, Tarbes 65016, France (e-mail: guillaume.vine@enit.fr; paul-etienne.vidal@enit.fr).

J.-M. Dienot is with the Laboratoire des Sciences de l'Ingenieur Appliquees a la Mecanique et au Genie Electriques–Federation IPPRA, Université de Pau et des Pays de l'Adour, Pau 64000, France (e-mail: Jean-Marc.dienot@iut-tarbes.fr).

Color versions of one or more of the figures in this paper are available online at http://ieeexplore.ieee.org.

Digital Object Identifier 10.1109/TPEL.2019.2916261

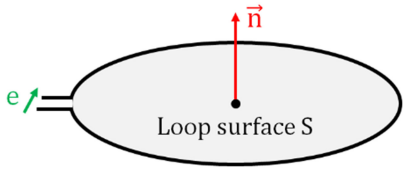

Fig. 1. Ideal loop antenna.

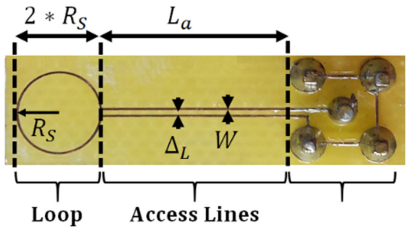

Fig. 2. Designed antenna prototype.

some experimental measurements that can be obtained from the antenna. Others graphics illustrate how the registered data can be used to compute some key parameters and variables of the power assembly.

II. Loop Passive Antenna and Measurement Chain for NF Investigation

A. General Theoretical Background

An elementary magnetic probe, represented in Fig. 1, can be modeled as a conductive loop antenna. Immersed in a magnetic field $\vec{H}$, the antenna operates on the principle of inductive coupling. The time variation of the magnetic flux Φ through the loop surface S induces an electromotive force e at its terminal (1). $\mu_0 = 4\pi * 10^{-7}$ H.m^{-1} corresponds to the permeability of the non-magnetic media surrounding the loop

$$e = -\frac{d\phi}{dt}, \quad \phi = \mu_0 * \iint_S \vec{H}.\vec{n} * dS. \tag{1}$$

If the loop surface is sufficiently small, the magnetic field can be considered homogeneous within. The induced electromotive force can be linked to the normal component of the magnetic field at the center of the loop H_{n0} in the frequency domain

$$e = j\omega * \mu_0 * \iint_S H_n * dS \approx j\omega * \mu_0 * S * H_{nO}. \tag{2}$$

In this condition, the sensor is similar to a punctual receiver and the relationship between the induced voltage at the loop's terminal and the incident magnetic field H_{n0} is expressed.

B. Antenna Design

In this paper, a circular form antenna realized in planar technology, copper on epoxy substrate is used. It is illustrated in Fig. 2. The probe is composed of: the circular loop of radius $R_S = 3$ mm, defined from the center to the middle of the track, and track width $W = 0.2$ mm; The access lines of length $L_a = 15$ mm, tracks width $W = 0.2$ mm, and a spacing from inner edges $\Delta L = 0.3$ mm; and the sub-miniature version subminiature version A (SMA) connector, which realizes the connection to the measuring instrument. The epoxy substrate thickness is 1.6 mm and the track thickness is 35 μm.

This antenna was developed in [7] in order to fulfill integration requirements of power electronic modules. In particular, the access lines are added to move the connector away from the measurement loop and the DUT. The line length is chosen according to the dimensions of the power demonstrator presented further in Section IV, as illustrated in Fig. 8.

C. Measurement Chain

It is noted that the SMA connector allows us to connect the antenna to a measuring instrument through an radio frequency (RF) coaxial cable.

To achieve real-time monitoring, the output voltage V_M of the antenna is monitored by an oscilloscope with a frequency bandwidth of 500 MHz. The measuring device accesses the voltage V_M across the measurement resistance$R_M = 50\ \Omega$. As a matter of fact, the 50-Ω input impedance of the oscilloscope is selected to fulfill the characteristic impedance of the coaxial cable. The analog-to-digital convertor resolution is 8-bit for a maximal signal voltage of 1 V.

D. Antenna Performances

Equation (2) highlights that the induced voltage is proportional to the area of the loop. Thus, the sensitivity improvement is at the expense of spatial accuracy [9]. Moreover, the antenna can be also subjected to an electrical coupling. This parasitic effect is significant at high frequencies and increases with the area of the loop. The sensitivity improvement is at the expense of the frequency bandwidth of the antenna too [10]. In general, the antenna design corresponds to a compromise between the three following performances of an NF magnetic investigation–sensitivity, spatial accuracy, and frequency bandwidth.

This compromise depends on the system under test and the constraints associated. The defined antenna performances are discussed twice in the following. Performances are analyzed with a preliminary study case. Then, the analysis is completed with power module NF investigation.

III. Model and Preliminary Study of the Loop Antenna

A. Modeling Objectives

An isolated antenna model based on the prototype design is developed. As it is designed for power electronic modules, its model and its characterization are developed and studied out over the frequency range 1 kHz$-$1 GHz. The results will be analyzed through a simulation and experimental comparison. Experimental results are produced, thanks to a vector network analyzer (VNA). It enables us to measure the input impedance Z of the antenna. The calibration of the measurement is carried out with a short-open-load kit at the termination of the RF cable. The antenna is 0.5 m away from any metal object to avoid coupling. According to the electromagnetic reciprocity, the antenna response in the receiver mode is deduced [11]. Therefore, the antenna is characterized in the transmitter mode.

On the basis of the RF coaxial cable datasheet, the waveform velocity in the cable is 2e8 m/s. In the considered frequency

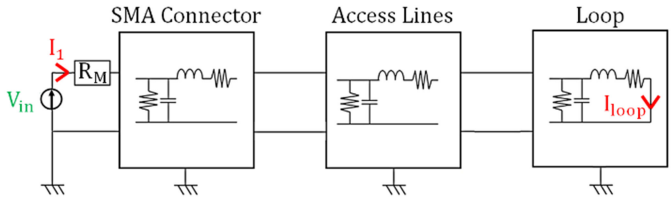

Fig. 3. Loop antenna simplified model.

bandwidth, the cable is equivalent to a pure delay, which is determined to be 4.6 ns. Experimental characterization not presented hereby validates it [12]. In the following section, the focus is on the integrated antenna modeling and characterization. The effect of the coaxial cable will be later inserted as a pure delay.

B. Antenna Model

To fulfill the electrical behavior, the antenna is divided in three parts: the loop, the transmission line, and the connector. The dimensions of each part allow us to consider a lumped element model over the studied frequency range. Thus, an equivalent *RLCG* circuit is established. The couplings between the three parts are inserted as mutual inductances and capacitors. A simplified model of the antenna is presented in Fig. 3.

The VNA is included and is represented by the input voltage V_{in} and the termination load $R_M = 50\ \Omega$. The complete model was established and is presented in [7]. It is noted that I_{loop} is the current flowing through the equivalent inductance of the loop, whereas I_1 is the current through R_M.

A 3-D Numerical Tool Q3D Extractor [13] is used to obtain the values of electrical parameters and coupling coefficients on the frequency range [1 kHz–1 GHz] with a 1 kHz frequency step.

C. Characterization of the Magnetic Antenna

1) Impedance Characterization: The model is used to compute the input impedance of the designed antenna denoted as Z, among the frequency range defined. The results are compared to experimental measurements. Under the assumption of free interaction, it is demonstrated that the antenna impedance behavior is inductive from 100 kHz to 1 GHz as illustrated in Fig. 4.

2) Antenna Factor: The antenna factor F_m corresponds to the antenna response in the receiver mode. F_m is defined in (3) where V_M corresponds to the output voltage of the antenna across the measurement resistance$R_M = 50\ \Omega$

$$F_m = \frac{V_M}{H_{nO}}. \tag{3}$$

Based on reciprocity principle, the previous model allows us to compute the receiver mode [14]. In receiver mode functioning, the F_m expression is simplified as given in (4), where the antenna input impedance Z and the currents I_{loop} and I_1 were computed previously

$$F_m = j\omega * \mu_0 * S * \frac{Z}{R_M + Z} * \frac{I_{\text{loop}}}{I_1}. \tag{4}$$

F_m is simulated and plotted in Fig. 5.

The cutoff frequency of 3 dB deviation f_c is identified to be 230 MHz. Compared to a normal magnetic field excitation, the

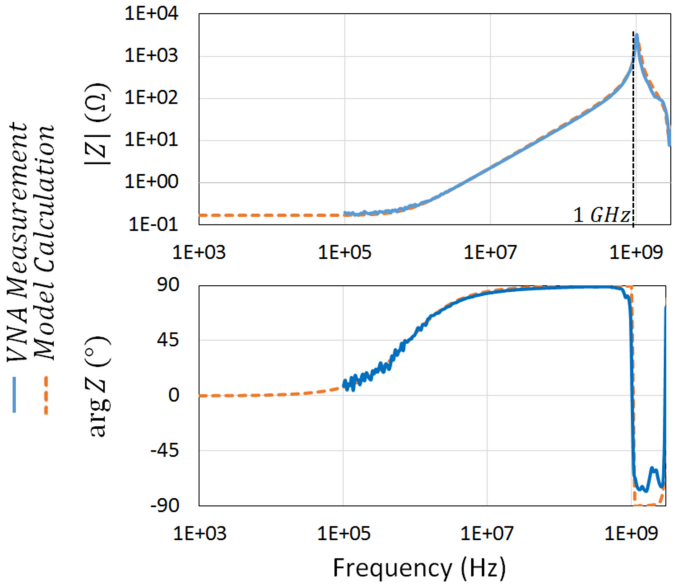

Fig. 4. Impedance behavior characterization of an antenna without coupling.

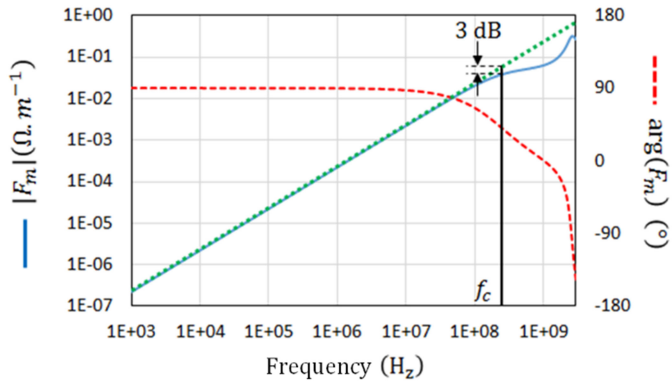

Fig. 5. Antenna factor computation.

frequency linear response of the antenna is thus assumed to be below 230 MHz.

This preliminary study is completed by the coupling characterization between two coplanar antennas, as source and receiver, in [7]. In this work, a complementary study was carried out to validate experimentally this antenna factor in a frequency bandwidth of 164 MHz. As a matter of fact, it is demonstrated that this higher limit is mainly due to parasitic electrical coupling occurring above this value. Some improvement designs are highlighted (guard ring …).

The conclusion is that the established model reproduces a correct behavior. Taking into account every constraint obtained leads to consider an antenna bandwidth of 1 kHz–164 MHz.

3) Antenna Transfer Synthesis: Finally, the coaxial cable between the SMA connector and the oscilloscope input is taken into account as a pure delay that is inserted as a multiplier of the antenna factor, as illustrated in Fig. 6. The normal magnetic field H_{nO} is computed with the antenna factor. Indeed, the V_M time measurement is computed by usual fast Fourier transform (FFT) algorithm. Then, the linear frequency-dependent antenna factor is applied to obtain the H_{nO} Fourier transform. Finally, if a time representation is needed, an inverse FFT is applied.

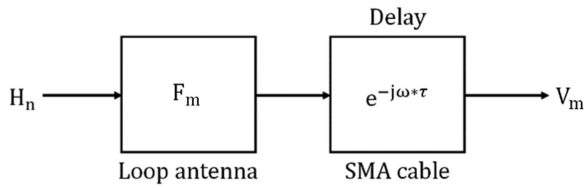

Fig. 6. Full measurement chain model.

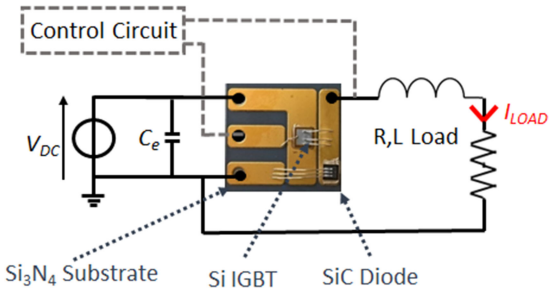

Fig. 7. Buck converter and its electrical connections.

IV. Power Electronic Device and Distrubances Analysis

The aim of the following section is to plot and analyze the results of the NF magnetic radiations from a dedicated power electronic device. The measurement setup is realized to extract the time and frequency characteristics of electromagnetic disturbances, taken at one measurement point, or as an overall surface distribution.

A. Presentation of the Power Bench

The studied converter is shown in Fig. 7. It is an elementary switching cell made of an silicon carbide (SiC) diode and a silicon (Si) insulated gate bipolar transistor (IGBT). They are brazed onto a silicon nitride substrate—Si3N4 with copper metallization. The converter is connected at the input to a dc voltage supply $V_{\mathrm{DC}} = 15$ V and a decoupling capacitance $C_e = 1$ mF. The output is connected to an inductive load composed by a resistance $R = 1.25\ \Omega$ and an inductance $L = 3$ mH. The IGBT is controlled by a bootstrap driver circuit at the switching frequency $f_{\mathrm{dec}} = 10$ kHz and the duty cycle $\alpha = 0.5$. At this operating point, the output current smoothed by the inductive load I_{LOAD} is equal to 6 A.

The operating conditions of the converter are mainly reduced for the applied voltage. The current rating of the diode and the IGBT are 1200 V–25 A. Indeed, in order to ease the positioning and the displacement of the loop antenna above the switching cell, the plastic packaging, the insulating gel, and the heat cooling system are not used.

In the following, the presented measures are performed over 50 switching periods with the averaging mode, which corresponds to an acquisition time of 5 ms.

B. Experimental Setup

The magnetic antenna is moved over the switching cell, thanks to a specific test support made by 3-D-additive manufacturing with thermoplastic polylactic acid, shown in Fig. 8. It consists

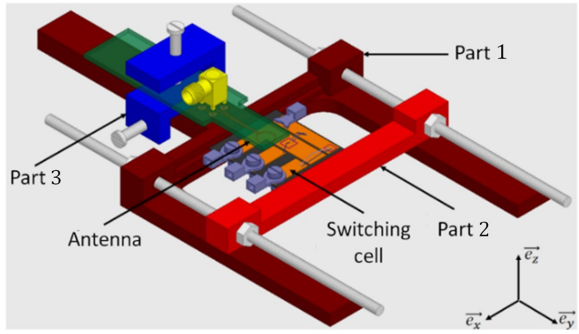

Fig. 8. Antenna test support.

of three parts and a set of screws and nuts, in Teflon, to fix the switching cell (parts 1 and 2) and to adjust the positioning of the antenna (part 3). All the materials are non-metallic and do not influence the radiation of the magnetic field from the DUT by skin or proximity effect.

This support is dedicated to the measurement of the H_z component of the magnetic field radiated by the switching cell. Part 3 is carried out to perform these measurements at the height $h = 0.5$ cm of the upper face of the substrate. The positioning is first visual and then adjusted using a vernier caliper. The antenna test support, illustrated in Fig. 8, is moved by hand.

A printed circuit board (PCB) made of epoxy FR4 with a thickness of 1.6 mm and copper tracks of 35 μm thick and 2 mm wide is designed to connect the switching cell to the load, driver, and dc source as illustrated in Fig. 9. The connection to A, B, C, and G terminals of the switching cell is made by copper stranded cables with a diameter of 2.5 mm. The PCB is placed at $z = 1.5$ cm of a ground plane. The antenna test support and the antenna are put above the PCB. One must pay attention on the initial $(x = 0, y = 0, z = 5$ mm$)$ position of the antenna compared to the switching cell. As a matter of fact, this initial point will be the origin of the measurement mapping.

The surface of the switching cell is scanned to measure the magnetic field in 37 positions detailed in Fig. 9. Every center of numbered circle denotes the xy coordinate where the center of the integrated antenna is positioned. The measurement steps in x and y are 4.5 and 5 mm, respectively, as illustrated with point 21 (x_{21}, y_{21}) in Fig. 9. To obtain the complete mapping — of 37 positions, the measurement time is 1 h. It is noted that, similar to the area of the loop, these measurement steps influence the spatial accuracy to identify and localize magnetic field sources, i.e., the conducted currents inside the switching cell. The spatial step separation between the measures can be adapted following measurement objectives.

To further interpret the data collected by this magnetic NF investigation, a three-step method is carried out: first, the identification of magnetic field sources, second, the current measurement and time analysis, and, finally, the magnetic field simulation.

C. Identification of Magnetic Field Sources

During its operation, the converter switches between two sequences related to the state of the IGBT: ON state and OFF state. The origins of electromagnetic disturbances are the high current

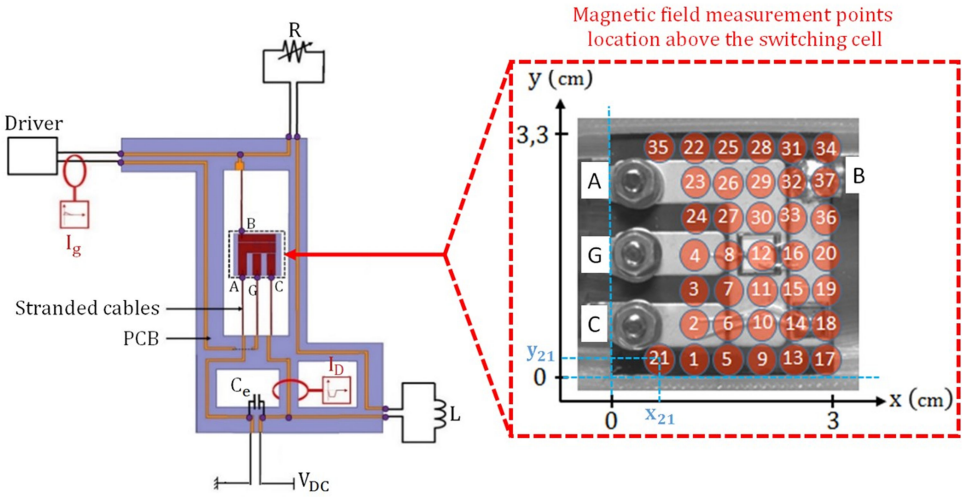

Fig. 9. Power converter bench test.

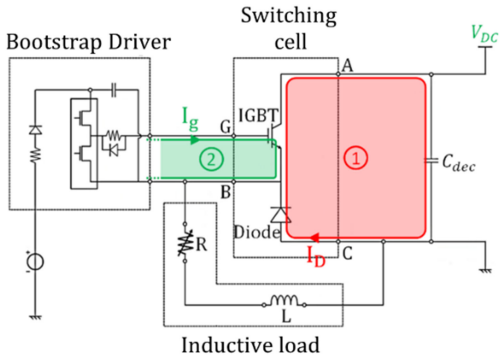

Fig. 10. Principal conducted DM disturbances.

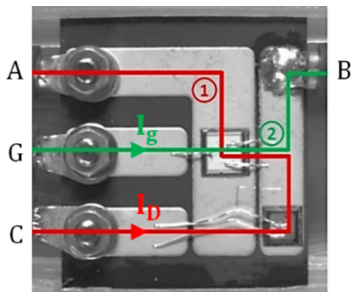

Fig. 11. Zoom view on the power active substrate.

and voltage gradients generated during the switching of power components, IGBT, and diode. These disturbances propagate through the conductors connecting the converter and are influenced by their parasitic elements (*R, L, and C*). They affect the reliability of the device with among others over-voltages, over-currents, and high-frequency resonances. The identification of these transient switching phenomena is the objective of the NF magnetic measurements.

Two modes of disturbances can be distinguished, the differential mode (DM) and the common mode (CM). In order to compare magnetic NF measurements to currents conducted measurements, the conclusions will be made for frequencies 10 kHz $\leq$ f $\leq$ 30 MHz. On the studied frequency band, the NF magnetic radiation is mainly due to DM disturbances. For this reason, the performed magnetic field measurements are intended primarily to analyze this mode of disturbances. It should be noted that, in general, electric antennas are more suitable for measuring CM phenomena [16].

The DM disturbances flow mainly through the power switching and the IGBT gate signal loops, which are represented in Fig. 10. Loop 1 is designated as the power switching loop (or the "hot loop"). Loop 2 is designated as the IGBT gate signal loop. During the turn-ON phase (respectively turn-OFF), high currents charge (respectively discharge) the input capacitance of the IGBT during a short time.

Other disturbance's paths can be considered, in particular, the load path. Above the switching cell, the conducted disturbances through these paths have less influence on the radiated magnetic field than paths 1 and 2. Since this paper is focused on switching cell wideband characterization, they are not investigated.

The propagation paths within the switching cell associated with these two loops are shown in Fig. 11. The spatial distribution and the temporal/frequency characteristics of the magnetic field radiated on the surface of the switching cell are supposed to be the image of these disturbances.

For a better understanding of the link between Figs. 10 and 11, the input/output ports of the switching cell A, B, C, and G are reported in both figures, as well as the currents I_D and I_g through the IGBT gate and the diode.

D. Conducted Currents Measurement

I_D and I_g are measured with a Rogowski coil and reported in Figs. 12 and 13. These measures give access to the fast transient disturbances flowing through these loops during IGBT turn-ON and turn-OFF phases. It is noted that the used Rogowski coil has a frequency bandwidth f_{ch} of 30 MHz.

Each switching sub-phase is numbered from one to eight. During the IGBT turn-ON phase, sub-phase 1 corresponds to the charging of the parasitic IGBT gate–emitter capacitance through the gate signal loop. Sub-phase 2 is the Miller plateau. IGBT starts switching ON, its current increases and flows through the

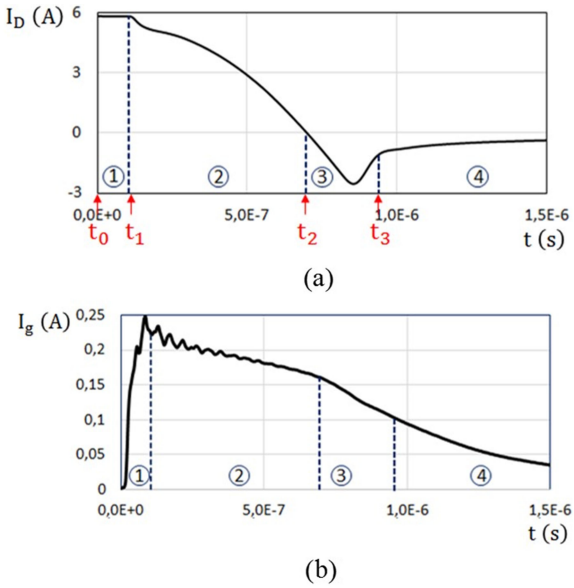

Fig. 12. Currents measurement during IGBT turn-ON phase. (a) Current through the power diode. (b) IGBT gate current.

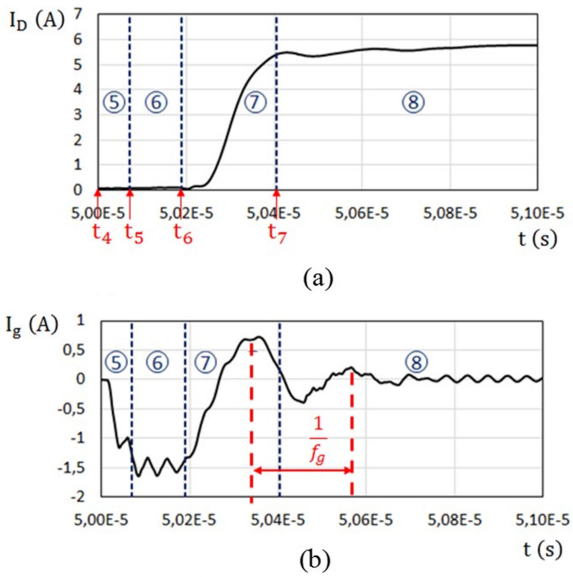

Fig. 13. Currents measurement during IGBT turn-OFF phase. (a) Current through the power diode. (b) IGBT gate current.

power switching loop. Sub-phase 3 corresponds to the diode reverse recovery. Sub-phase 4 is the end of the switching. During the IGBT turn-OFF phase, sub-phase 5 corresponds to the discharging of the parasitic IGBT gate–emitter capacitance. Sub-phase 6 is the Miller plateau. The collector–emitter voltage of the IGBT starts to increase. The current in the diode stays to zero. Sub-phase 7 corresponds to the diode switching ON, its current increases, and flows through the power switching loop. In the same time, the gate current I_g resonates at the frequency $f_g = 3.44$ MHz linked to the parasitic IGBT gate–emitter capacitance and the gate signal loop inductance. Sub-phase 8 is the end of the switching. These sub-phases are confirmed by the analysis of IGBT gate–emitter and collector–emitter voltages, which are not presented here.

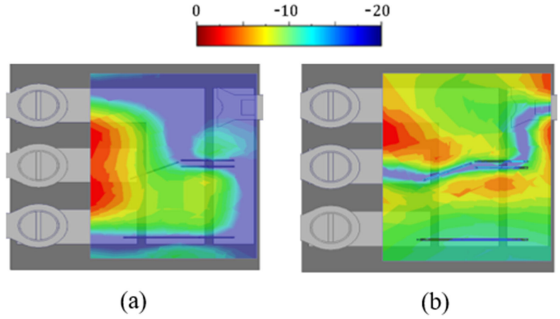

Fig. 14. H_z magnetic field simulation. (a) Power switching loop. (b) Gate signal switching loop.

The times t_0 to t_7 correspond to the delimitation of the sub-phases. It is noted that sub-phases 2 and 7 correspond to the current switching phases of the device. During these phases, the power switching loop is particularly radiant. The durations of these phases can be considered as the current switching times: $t_{\text{on}} = t_2 - t_1 = 497$ ns for the IGBT turn-ON phase and $t_{\text{off}} = t_7 - t_6 = 205$ ns for the IGBT turn-OFF phase.

E. Magnetic Field Simulation

The third step is the simulation of radiated magnetic field from the switching cell with the 3-D Numerical Tool Maxwell Ansys. Power and gate signal loops are successively fed by 100 MHz 1 A current. When the power switching loop is activated, the IGBT collector–emitter connection is short-circuited and the diode is switched ON. When the gate signal loop is activated, the IGBT gate–emitter connection is short-circuited and the diode is switched OFF. The associated simulation of magnetic field H_z distributions is reported in Fig. 14. H_z is figured in dB unit with normalization to the maximum value. These results will be compared later to experimental measurements.

The simulation results highlight that the H_z field distribution is related to the current paths represented in Fig. 11. Indeed, the H_z component is minimal above the associated current path.

V. Experimental Results

In a previous study [12], it was demonstrated how magnetic field measurements allow identifying basic characteristics of the power device behavior: period, duty cycle, and switching times. Based on improved result representations, new characterizations are described hereby. The analysis is carried out based on magnetic mappings, temporal transient representations, and spectral distributions at given positions. The discussion will highlight a method to exploit the results for every representation with the idea of application-oriented *in situ* magnetic field measurement.

A. Energy Temporal Density Mapping

For each position, the temporal energy density of the signal measured across the antenna, $|V_{\text{out}}(t)|^2$, is computed. Based on it, the signal energy during a time interval $[t_i, t_i + \Delta t]$, (5), is considered. E_{vout} is calculated from $|V_{\text{out}}(t)|^2$ for switching sub-phases 1 to 8 with time intervals identified by the currents measurement shown in Figs. 12 and 13. The E_{vout} calculation for a given sub-phase is done with $t_i \in \{t_0, \ldots, t_7\}$ and Δt

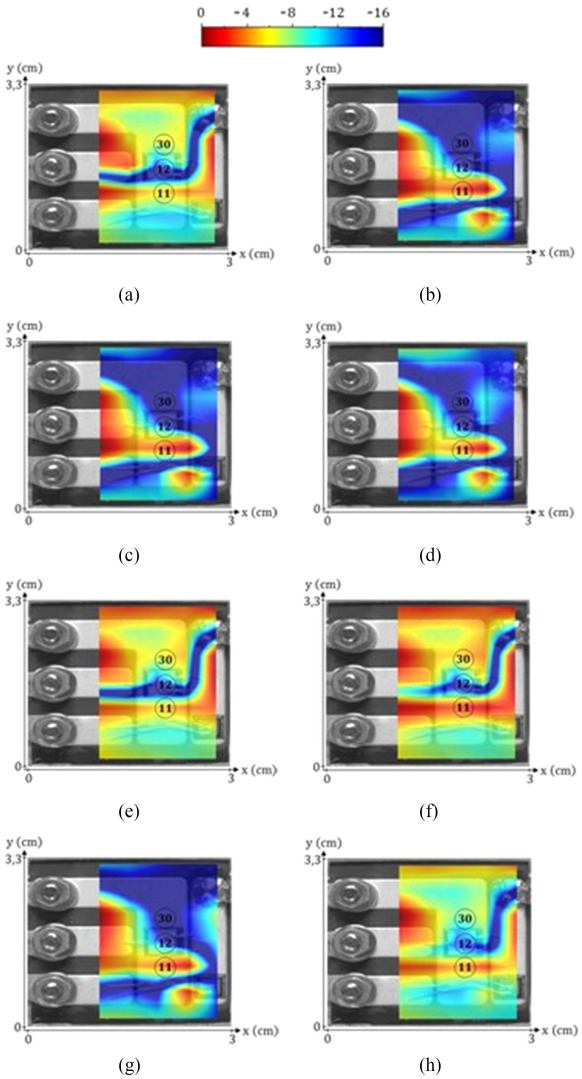

Fig. 15. Energy of the measured signal during the eight switching phases. (a) Phase 1. (b) Phase 2. (c) Phase 3. (d) Phase 4. (e) Phase 5. (f) Phase 6. (g) Phase 7. (h) Phase 8.

corresponding to the duration of the sub-phase. The results are reported in Fig. 15. The magnitude of E_{vout} is plotted in a mapping form with the use of a bi-linear interpolation. A normalization to the maximum value and a dB unit scale are used

$$\mathrm{E}_{\text{vout}}\ [t_i, t_i + \Delta t] = \int_{t_i}^{t_i+\Delta \mathrm{t}} |V_{\text{out}}(t)|^2 * dt. \tag{5}$$

These maps the propagation paths of conducted disturbances within the switching cell for each phases. They can be compared to those simulated previously, shown in Fig. 14. Indeed, as an illustration, for phases 1 and 5, the E_{vout} mapping is typical of the gate signal loop as highlighted in Fig. 14(b). This result was expected. As a matter of fact, during these phases, the gate current varies rapidly unlike the current through the power loop. Thus, the gate signal loop radiates. Similarly, during the phases 2, 6, and 7, it is identifiable that the E_{vout} map is typical of the power loop. This is consistent with the analysis performed on conducted waveforms. In general, it is identifiable that the map obtained for each phases can be associated to conducted

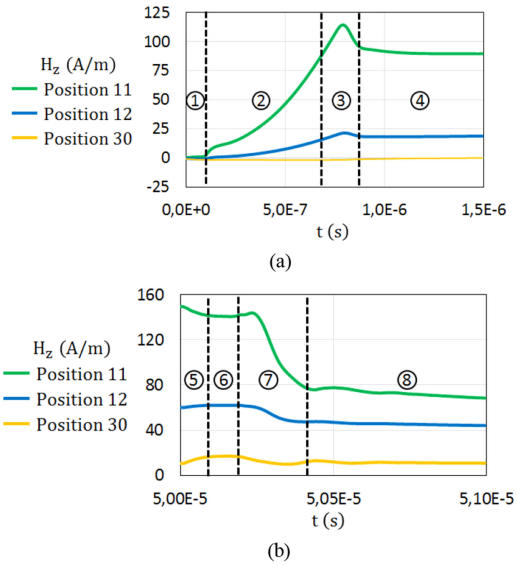

Fig. 16. Zoom view of the magnetic field detected. (a) IGBT turn-ON phase. (b) IGBT turn-off phase.

disturbances through the gate signal loop or through the power loop.

The differences between H_z map simulations and E_{vout} measurements can be related to the limited spatial accuracy of this NF investigation and to imprecisions in the numerical modeling of the power device. However, the measurements carried out make it possible to identify and localize DM conducted disturbances. For these objectives, it is stated that the spatial step separation taken was adapted.

These maps also make it possible to identify high and low magnetic coupling spots between the loop antenna and the DUT. These spots are related to the design of the system and reveal the best location for an integrated antenna. For instance, as illustrated in Fig. 15, the position 11 is a hot spot for both loops. The position 12 is a place of weak radiation for the IGBT gate loop. The position 30 is a place of weak radiation for the power switching loop. Antenna integration at these positions is discussed in the following section.

B. H_z Radiated-Field Temporal Representation

By the use of the full measurement chain model, shown in Fig. 6, H_z is computed and plotted for the three positions mentioned previously, as illustrated in Fig. 16.

At position 11, the measured waveform corresponds to the superposition of the transient phenomena linked to the two loops previously described. This allows observing the eight switching sub-phases depicted above. This is one of the benefits of having an integrated magnetic sensor. The choice of this single measurement can be done according to the previous mapping of Fig. 15. Indeed, position 11 is a good candidate. As a matter of fact, for monitoring similar phases, it is necessary to measure two currents as plotted in Figs. 12 and 13.

At positions 12 and 30, the measured waveforms are respectively similar to the measured currents I_D and I_g as illustrated in Figs. 17 and 18. Indeed, the weak coupling between the antenna and, the IGBT gate loop, the power switching loop, at the

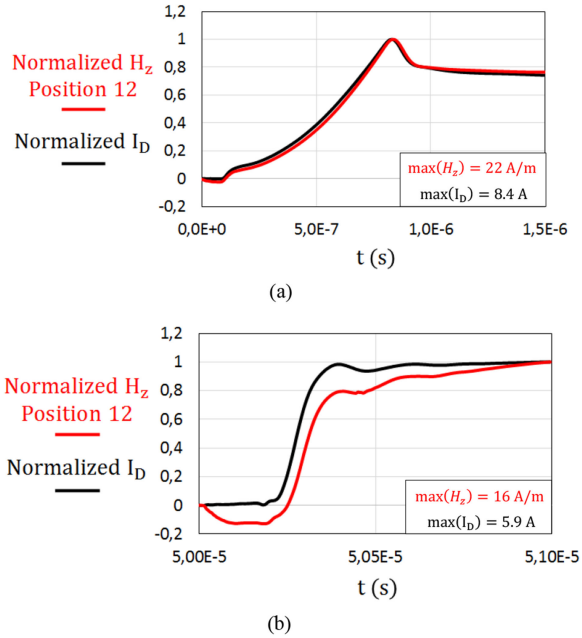

Fig. 17. Comparison between the measurements of H_z in position 12 and the current through the diode. (a) IGBT turn-ON measurements. (b) IGBT turn-OFF measurements.

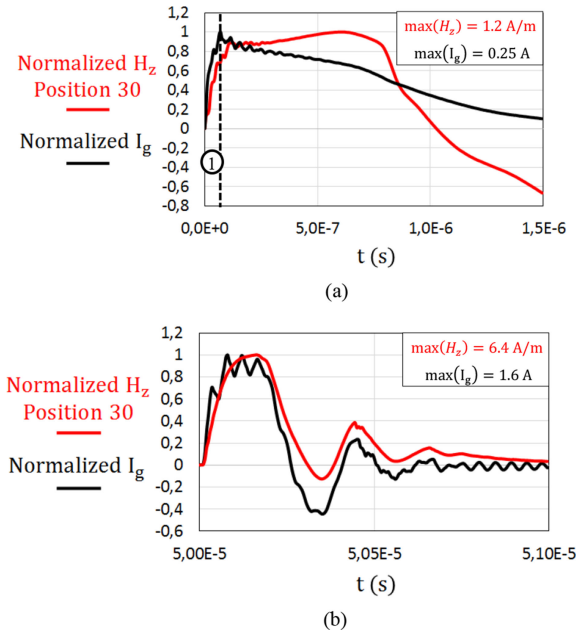

Fig. 18. Comparison between the measurements of H_z in position 30 and the current through the IGBT gate. (a) IGBT turn-ON measurements. (b) IGBT turn-OFF measurements.

position 12 and position 30, respectively, allows observing the conducted disturbances associated to the other loop. However, due to low amplitude of the gate current, the magnetic field measurement at position 30 also takes into account the I_D current radiation. As illustrated in Fig. 18(a), during phase 1, H_z reproduces the gate current waveform. Following that phase, the I_D current increases and affects the measure.

Magnetic field measurements provide access to switching details, propagation paths of DM disturbances, and radiation

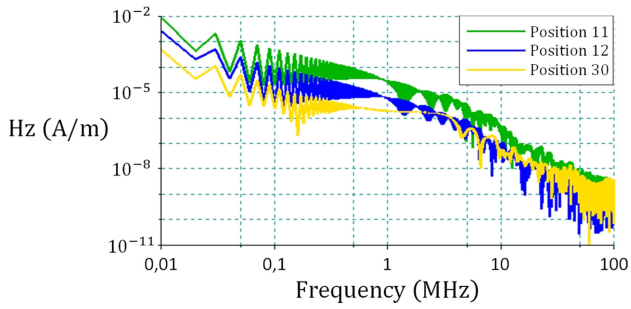

Fig. 19. FFT of H_z.

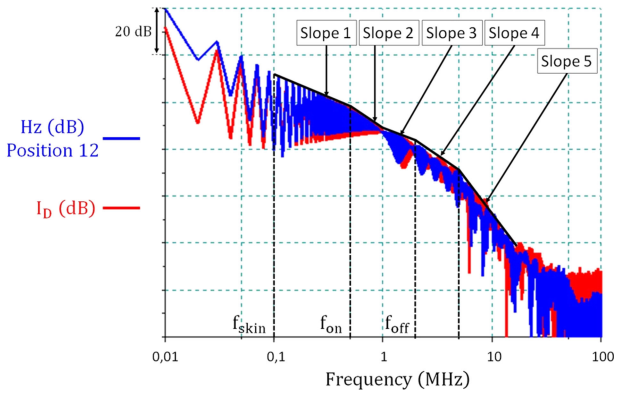

Fig. 20. Spectral distribution comparison between the measurements of H_z in position 12 and the current through the diode.

distribution. The frequency-domain analysis of the measured disturbances is carried out in the following section.

C. H_z Radiated-Field Spectral Representation

The FFT for each position is computed from V_{out} measurement and gives access to the spectral distribution of magnetic field. Fig. 19 depicts the FFT of the magnetic field computed from the time measurements for positions 11, 12, and 30.

First, it is noted that position 11 is a hot spot for both disturbance loops. This explains that monitored amplitudes have greater values than other points.

Second, the magnetic field received at position 12 is mainly generated through the power switching signal as identified previously in the time domain. Fig. 20 depicts the measurements of H_z in position 12 and the current through the diode in the frequency domain. To compare the two spectral envelopes, a per position relative scale in dB is used. The spectral envelope of the magnetic field in the frequency range from f_{skin} to 30 MHz is similar to the conductive disturbances in the power loop. f_{skin} corresponds to the skin effect frequency of the power substrate copper tracks defined in (6) where $e = 300\ \mu\text{m}$ is the conductor thickness, $\sigma = 59.6 * 10^6\ \text{S/m}$ is the copper conductivity [17]. Below this value, the copper tracks cannot be considered as a perfect conductor and couplings between current loops and the antenna are frequency dependent

$$f_{\text{skin}} = \frac{1}{(e)^2 * \pi * \sigma * \mu_0}. \tag{6}$$

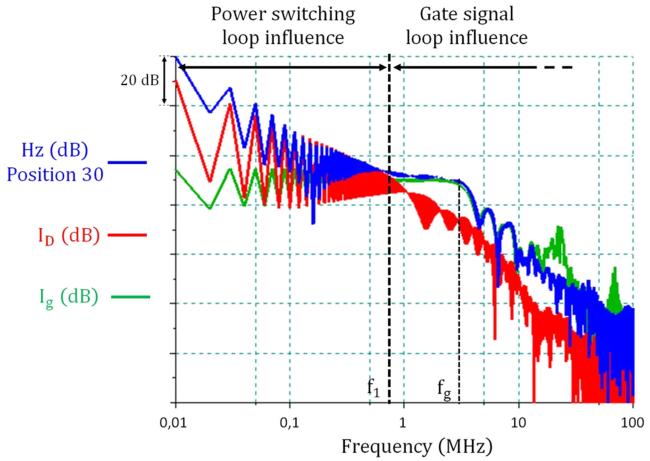

Fig. 21. Spectral distribution comparison between the measurements of H_z in position 30, the current through the diode, and the current through the IGBT gate.

Spectrum envelopes are related to transient waveforms and their characteristic times. This is illustrated in [18] where the authors determine analytically the spectrum envelope of a trapezoidal waveform, which is representative of the power loop signal. Indeed, the paper defined two cutoff frequencies associated to the rise time $t_{\rm on}$ and fall time $t_{\rm off}$ times of the trapezoid. The considered relationships are $f_{\rm on} = \frac{1}{\pi * t_{\rm on}}$ and $f_{\rm off} = \frac{1}{2 * t_{\rm off}}$. As a matter of fact, the waveform during the IGBT turn-ON is assimilated to a constant slope function. During turn-OFF, the waveform is considered to be of type of the following transient function as defined in [18]

$$T_R(t) = \frac{\left(1 - \cos\left(\frac{\pi * t}{t_{\rm off}}\right)\right)}{2}. \tag{7}$$

By considering the value of $t_{\rm on}$ and $t_{\rm off}$ obtained previously in Figs. 12 and 13, the cutoff frequencies associated to the DUT are $f_{\rm on} = 497$ kHz and $f_{\rm off} = 2.43$ MHz. They are reported in Fig. 20 and allow to reveal envelope slope changes. For instance, five different slopes are distinguished. At this position, the measured radiated field gives access to the characteristic frequencies of the power switching loop.

Finally, Fig. 21 depicts the measured magnetic field at position 30. As monitored in Fig. 21, below the frequency $f_1 = 750$ kHz, the magnetic field received is due mainly to the power switching loop, whereas, above f_1, it is related to the gate signal loop with a specific resonant frequency $f_g = 3.44$ MHz. f_g was defined in Section IV-D and corresponds to the gate current resonance during IGBT turn-OFF phase. The bootstrap driver added to a large gate signal loop enforces the H_Z magnitude at f_g. Then, in the frequency range from f_1 to 30 MHz, the radiated-field spectral envelope is close to the spectral envelope of the gate signal loop I_g. At this position and for frequencies greater than f_1, the measured radiated field gives access to characteristic frequencies of the gate switching loop.

More generally, for a given electromagnetic disturbance to monitor, the antenna position should be well adapted. Based on that work, it has been demonstrated that following the antenna position, the spectral envelope of the measured H_Z is directly connected to a given disturbance loop. For instance, position 12 is linked to the power switching loop. In position 30, both power switching and gate signal loops are highlighted following the characteristic frequency f_1.

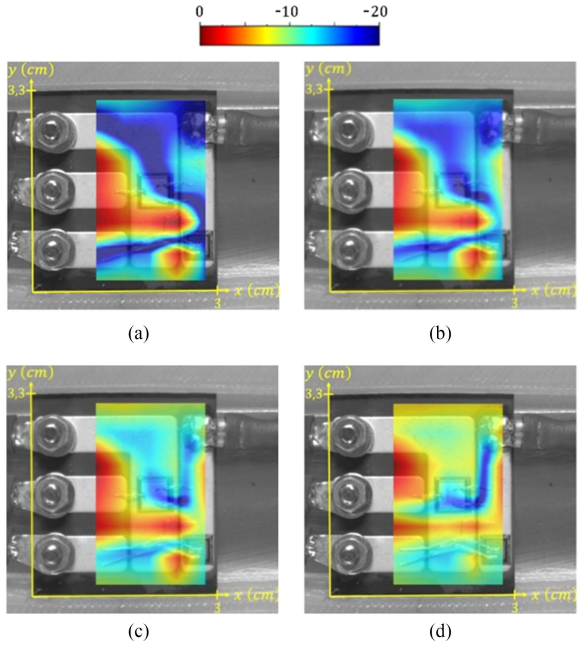

Fig. 22. Magnetic field distribution. (a) 10 kHz − 1 MHz. (b) 1 − 10 MHz. (c) 10 − 30 MHz. (d) 30 − 100 MHz.

D. Energy Spectral Density Mapping

The experimental setup allows to move the antenna above the top area of the power device. The spectral density is plotted at every position in Fig. 22. The spectral density is defined by

$$\int |fft(H_z)|^2 df. \tag{8}$$

The spectral density is plotted for several frequency ranges. Fig. 22(a) is obtained for 1 kHz $\leq f \leq$ 1 MHz, 22(b) is obtained for 1 MHz $\leq f \leq$ 10 MHz, 22(c) is obtained for 10 MHz $\leq f \leq$ 30 MHz, and 22(d) is obtained for 30 MHz $\leq f \leq$ 100 MHz. A bilinear interpolation is used to plot H_z map.

Fig. 22(a) and (b) highlights the main influence of the power switching loop for these frequencies. In Fig. 22(d), for higher frequencies, the gate signal loop is revealed as the main path for the current flow. In between, both paths can be detected. Indeed, frequency bandwidths of the magnetic field monitored are associated with conducted disturbances. Consequently, they are related to specific conductive disturbance paths. As these disturbances are linked to the power module technology and geometry, the influence of a design could be studied.

VI. Conclusion

This paper illustrates how near magnetic field characterization eases the wideband frequency electromagnetic behavior of power electronic modules. Measurements and analyses of near

magnetic field, radiated by a power electronic module, are presented. To achieve measurements, specific magnetic loop antennas are designed and depicted. An elementary sensor design is used in the idea of future integration within a power electronic module. Furthermore, antenna characterizations, which allow exploiting the output sensor data, are given. The antenna factor expression is established. Finally, the sensor measurements are presented and commented. It is highlighted that some specific power switching characteristics can be recovered. More precisely, the influence of the power switching loop and the IGBT gate signal loop are discussed. Time and frequency analyzes are provided. Finally, an experimental top distribution map of the radiated magnetic field is plotted. It is demonstrated how its frequency bandwidths are related to conducted disturbances.

More generally, the representation tools and analysis based on *in situ* magnetic field measurement can be enriched as this paper demonstrates the interest of integrated magnetic sensors.

For further studies, the prototype will be completed with a cooling system, plastic packaging, and silicone gel. Similar method will be used and focused on how to better exploit the H_z magnitude associated with frequencies, to reveal potential changes within the assembly process or during the functioning of the power device.

REFERENCES

[1] C. DiMarino, D. Boroyevich, R. Burgo, M. Johnson, and G-Q. Lu, "Design and development of a high-density, high-speed 10 kV SiC MOSFET module," in *Proc. 19th Eur. Conf. Power Electron. Appl.*, Warsaw, Poland, 2017, pp. P.1–P.10.

[2] L. Beghou, F. Costa, and L. Pichon, "Detection of electromagnetic radiations sources at the switching time scale using an inverse problem-based resolution method—Application to power electronic circuits," *IEEE Trans. Electromagn. Compat.*, vol. 57, no. 1, pp. 52–60, Feb. 2015.

[3] V. Kraz, "Near-field methods of locating EMI sources," in *Proc. RF EXPO WEST Conf.*, May/Jun. 1995, pp. 392–397.

[4] D. Baudry, A. Louis, and B. Mazari, "Overview of emission and susceptibility investigation and modeling with near-field measurements," Int. Union Radio Sci. General Assembly, Chicago, IL, USA, 2008.

[5] Y. Chen, X. Pei, S. Nie, and Y. Kang, "Monitoring and diagnosis for the DC–DC converter using the magnetic near field waveform," *IEEE Trans. Ind. Electronics*, vol. 58, no. 5, pp. 1634–1647, May 2011.

[6] G. Lourdel, J. M. Dienot, and E. Dutarde, "Integrated near-field probes for power switch Aln structure," Brevet FRA0405299, Mai 2004, Int. Patent Extension, USA, Jun. 2005.

[7] G. Viné, J.-M. Dienot, and P.-E. Vidal, "Theoritical and experimental study of magnetic sensors for near-field emission measurement. application to design and integration in power printed board circuit," in *Proc. Int. Symp. Electromagn. Compat.*, Angers, France, Sep. 4–8, 2017, pp. 1–6.

[8] I. Abari, A. Lahouar, M. Hamouda, J. B. H. Slama, and K. Al-Haddad, "Fault detection methods for three-level NPC inverter based on DC-bus electromagnetic signatures," *IEEE Trans. Ind. Electron.*, vol. 65, no. 7, pp. 5224–5236, Jul. 2018.

[9] S. Iskra and I. P. MacFarlane, "H-field sensor measurement errors in the near-field of a magnetic dipole source," *IEEE Trans. Electromagn. Compat.*, vol. 31, no. 3, pp. 306–311, Aug. 1989.

[10] C. F. M. Carobbi and L. M. Millanta, "Analysis of the common-mode rejection in the measurement and generation of magnetic fields using loop probes," *IEEE Trans. Instrum. Meas.*, vol. 53, no. 2, pp. 514–523, Apr. 2004.

[11] J. J. Goedbloed, "Reciprocity and EMC measurements," in *Proc. Int. Symp. Electromagn. Compat*., 2003, pp. 1–12.

[12] G. Vine, "Études et développements de capteurs électromagnétiques large-bande en vue de leur intégration dans des architectures d'électronique de puissance," Ph.D. dissertation, Toulouse INP, Toulouse , France, 2018, pp. 128–130.

[13] Parasitic element softaware extraction: Q3D Extractor. [Online]. Available: https://www.ansys.com/products/electronics/ansys-q3d-extractor, Accessed on: May 17, 2019.

[14] M. Ishii and K. Komiyama, "A measurement method for the antenna factor of small loop antenna by measuring the input impedance," in *Proc. Conf. Precis. Electromagn. Meas.*, London, U.K., 2004, pp. 80–81.

[15] G. Vine, P.-E. Vidal, and J.-M. Dienot, "Electromagnetic antenna for power electronic modules: Towards a real time electromagnetic characterization," in *Proc. 19th Eur. Conf. Power Electron. Appl.*, Warsaw, Poland, 2017, pp. P.1–P.10.

[16] A. Salceanu, C. Sarmasanu, and M. Cretu, "An approach for near-field measurement of radiated emissions from digital circuits," in *Proc. 11th IMEKO TC4 Symp. Trends Electr. Meas. Instrum.*, Lisbon, Portugal, 2001, pp. 28–31.

[17] J. C. Rautio and V. Demir, "Microstrip conductor loss models for electromagnetic analysis," *IEEE Trans. Microw. Theory Techn.*, vol. 51, no. 3, pp. 915–921, Mar. 2003.

[18] F. Costa and D. M. Member, "Graphical analysis of the spectra of EMI sources in power electronics," *IEEE Trans. Power Electron.*, vol. 20, no. 6, pp. 1491–1498, Nov. 2005.

Guillaume Vine received the Dipl.-Ing. degree in electronics from the Grenoble Institute of Technology, Grenoble, France, in 2014, and the Ph.D. degree in electrical engineering from the Toulouse Institute of Technology, Toulouse, France, in 2018.

Since 2018, he has been a Temporary Lecturer and Researcher with the Laboratoire Génie de Production, Toulouse University, Toulouse, France. His current research interests include near-field measurement and modeling techniques for power converters.

Paul-Etienne Vidal received the Ph.D. degree from the Institut National Polytechnique de Toulouse, Toulouse, France, in 2004. He received the Habilitation à Diriger des Recherches from the Institut National Polytechnique de Toulouse in 2017.

From 2004 to 2006, he was a Temporary Researcher with the Laboratory LEEI, INP/CNRS. Since 2006, he has been an Associate Professor with the Laboratoire Génie de Production, Toulouse University, Toulouse, France. His research interests include power converter efficiency. He developed three research themes within the PRIMES platform (http://www.primes-innovation.com/) facilities–electro- and thermo-mechanical modeling and simulations, experimental technology integration for power electronic device, and control strategy of power converters.

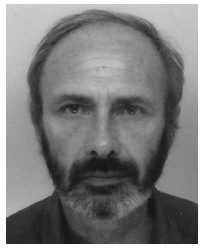

Jean-Marc Dienot (M'99) received the Ph.D. degree in microwave circuits and applied electromagnetic from the University Paul Sabatier, Toulouse, France.

He is currently a University Professor with the Institute of Technology, Tarbes, France. Since 1995, he has been interested and involved in new electromagnetic interferences and problematics in electronics' architectures and chips. He has developed and leads the LABCEEM, a scientific platform dedicated for research and high-level training projects in EMI and EMC domains. He is the author or co-author of more than 90 contributions in journals, books, and conferences.

Dr. Dienot is the recipient of scientific certifications in domains such as electronic power, EMC, instrumentation, and communications. He is currently with the Laboratoire des Sciences de l'Ingénieur Appliquées à la Mécanique et au Génie Electriques–Fédération, IPPRA, Pau, France.